Inhomogeneous inflation: Numerical evolution

Hannu Kurki-Suonio
Department of Theoretical Physics, University of Helsinki, 00014 Helsinki, Finland
and University of California, Lawrence Livermore National Laboratory, Livermore, California 94550

Pablo Laguna
Department of Astronomy and Astrophysics, The Pennsylvania State University, University Park, Pennsylvania 16802

Richard A. Matzner
Center for Relativity, The University of Texas at Austin, Austin, Texas 78712
(Received 24 May 1993)

We describe our three-dimensional numerical relativity code for the evolution of inhomogeneous cosmologies. During the evolution, the constraint equations are monitored but not solved. The code has been tested against perturbation theory with good results. We present some runs of inhomogeneous inflation with strongly inhomogeneous initial data.

PACS number(s): 04.20.Me, 98.80.Cq

I. INTRODUCTION

Inflation [1,2] has become the favorite explanation for both the large-scale homogeneity and the small-scale inhomogeneity of the Universe. The recent observation of the cosmic microwave anisotropy by the Cosmic Background Explorer (COBE) satellite [3] is consistent with the inflationary Universe scenario. Most work on inflation has been in the context of either a flat background spacetime or perturbation theory. A consistent general-relativistic treatment of strongly inhomogeneous inflation appears to require numerical relativity.

Previous numerical relativity calculations of inhomogeneous inflation have been one dimensional [4–7]. We have written a three-dimensional numerical relativity code for this purpose. The code consists of two parts. The first part solves the initial value problem. We described it in Ref. [8], where the motivation and background of this project are also discussed.

Here we present the second part, the evolution code. The main focus of this paper is on the code rather than physical conclusions about inhomogeneous inflation. Thus we discuss the evolution equations (Sec. II), numerical techniques (Sec. III), and code tests (Sec. IV). In Sec. V we present a couple of strongly inhomogeneous inflation runs.

II. EVOLUTION EQUATIONS

We derive evolution equations for general relativity with scalar field dynamics in a form suitable for numerical solution. They will be in the 3+1 formalism [9] and for a general gauge.

The matter source is a scalar field. The covariant form of the field equation is

$$g^{\mu\nu}\phi_{;\mu\nu}=V'(\phi)\ , \tag{2.1}$$

where $V(\phi)$ is a potential function, the form of which we are not restricting. The prime denotes a derivative with respect to the argument. Also, the semicolon denotes a covariant derivative with respect to the four-metric $g_{\mu\nu}=h_{\mu\nu}-n_\mu n_\nu$, and D_μ is the covariant derivative with respect to the three-metric $h_{\mu\nu}$. Here n^μ is the unit normal vector to the three-space slice, for which $n^\mu n_\mu=-1$, and $n^\mu h_{\mu\nu}=0$ (Greek letter indices range and sum over 0–3; Latin letter indices over 1–3). Since

$$h^{\mu\nu}\phi_{;\mu\nu}=D_\mu D^\mu\phi+Kn^\mu\partial_\mu\phi \tag{2.2}$$

and

$$\begin{aligned} n^\mu n^\nu\phi_{;\mu\nu}&=n^\nu\partial_\nu(n^\mu\partial_\mu\phi)-n^\nu n^\mu_{;\nu}\partial_\mu\phi \\ &=n^\nu\partial_\nu\eta+n^\nu\partial_\mu\phi(K^\mu_\nu+a^\mu n_\nu) \\ &=n^\nu\partial_\nu\eta-\frac{1}{\alpha}h^{\mu\nu}\partial_\mu\alpha\,\partial_\nu\phi\ , \end{aligned} \tag{2.3}$$

Eq. (2.1) becomes

$$D_\mu D^\mu\phi+K\eta-n^\nu\partial_\nu\eta+\frac{1}{\alpha}h^{\mu\nu}\partial_\mu\alpha\,\partial_\nu\phi=V'(\phi)\ . \tag{2.4}$$

Here we have defined a new variable

$$\eta\equiv n^\mu\partial_\mu\phi \tag{2.5}$$

to replace a second-order equation (2.1) with two equations [(2.4) and (2.5)] first order in time.

Hereafter we use 3+1 coordinates

$$(t,x^1,x^2,x^3)=(t,x,y,z)\ ,$$

with the metric [9]

$$ds^2=-\alpha^2dt^2+h_{ij}(dx^i+\beta^i dt)(dx^j+\beta^j dt)\ . \tag{2.6}$$

The scalar field equations just derived are now

$$\begin{aligned} \frac{1}{\alpha}(\partial_t-\beta^k\partial_k)\eta&=\frac{1}{\sqrt{h}}\partial_i(\sqrt{h}\,h^{ij}\partial_j\phi)+K\eta \\ &\quad+\frac{1}{\alpha}h^{ij}\partial_i\alpha\,\partial_j\phi-V'(\phi) \end{aligned} \tag{2.7}$$

and

$$\frac{1}{\alpha}(\partial_t-\beta^k\partial_k)\phi=\eta \ . \tag{2.8}$$

The 3+1 form of the Einstein equations is

$$R+K^2-K_{ij}K^{ij}=16\pi G\rho_H \ , \tag{2.9}$$

$$D_iK^i_j-D_jK=8\pi GS_j \ , \tag{2.10}$$

$$\partial_tK^i_j=-D^iD_j\alpha+\alpha[R^i_j+KK^i_j-8\pi GS^i_j+4\pi G\delta^i_j(S-\rho_H)] +\beta^k\partial_kK^i_j-K^k_j\partial_k\beta^i+\partial_j\beta^kK^i_k \ , \tag{2.11}$$

$$\partial_th_{ij}=-2\alpha K_{ij}+D_i\beta_j+D_j\beta_i \ . \tag{2.12}$$

Here R and R^i_j are the Ricci scalar and tensor of the three-metric, and G is Newton's constant. Equations (2.9) and (2.10) are the Hamiltonian and momentum constraints. We do not concern ourselves with the solution of the constraint equations in this paper as we have discussed it elsewhere [8].

For a scalar field, the source terms in Eqs. (2.9)–(2.12) will be

$$\rho_H=\tfrac{1}{2}h^{ij}\partial_i\phi\,\partial_j\phi+\tfrac{1}{2}\eta^2+V(\phi) \ , \tag{2.13}$$

$$S^j=-\eta h^{ij}\partial_j\phi \ , \tag{2.14}$$

$$S^{ij}=h^{ij}[-\tfrac{1}{2}h^{kl}\partial_k\phi\,\partial_l\phi+\tfrac{1}{2}\eta^2-V(\phi)] +h^{ik}h^{jl}\partial_k\phi\partial_l\phi \ , \tag{2.15}$$

$$S\equiv S^i_i=-\tfrac{1}{2}h^{ij}\partial_i\phi\,\partial_j\phi+\tfrac{3}{2}\eta^2-3V(\phi) \ . \tag{2.16}$$

The evolution equation for the extrinsic curvature, Eq. (2.11), becomes

$$\frac{1}{\alpha}(\partial_t-\beta^k\partial_k)K^i_j=KK^i_j-\frac{1}{\alpha}h^{ik}(\partial_j\partial_k\alpha-\Gamma^l_{jk}\partial_l\alpha)+R^i_j -8\pi G[h^{ik}\partial_k\phi\,\partial_j\phi+\delta^i_jV(\phi)] +\frac{1}{\alpha}(K^i_k\partial_j\beta^k-K^k_j\partial_k\beta^i) \ . \tag{2.17}$$

We shall evolve the trace $K\equiv K^i_i$ and the traceless part $A^i_j\equiv K^i_j-\frac{1}{3}\delta^i_jK$ separately. The evolution equation for the trace is

$$\frac{1}{\alpha}(\partial_t-\beta^k\partial_k)K=K^2-\frac{1}{\alpha\sqrt{h}}\partial_i(\sqrt{h}\,h^{ij}\partial_j\alpha)+R -8\pi Gh^{ij}\partial_i\phi\,\partial_j\phi-24\pi GV(\phi) \ . \tag{2.18}$$

Using

$$D_i\beta_j=\partial_i\beta_j-\tfrac{1}{2}\beta^l(\partial_jh_{li}+\partial_ih_{lj}-\partial_lh_{ij}) \ , \tag{2.19}$$

the three-metric evolution equation, Eq. (2.12), becomes

$$\frac{1}{\alpha}(\partial_t-\beta^k\partial_k)h_{ij}=-2K_{ij}+\frac{1}{\alpha}(h_{ki}\partial_j\beta^k+h_{kj}\partial_i\beta^k) \ . \tag{2.20}$$

It turns out to be useful to have a separate evolution equation for the square-root of the determinant of the three-metric, $\sqrt{h}$. Using

$$\frac{1}{\sqrt{h}}\partial_t\sqrt{h}=\frac{1}{2}h^{ij}\partial_th_{ij} \tag{2.21}$$

with Eq. (2.12) we get

$$\frac{1}{\alpha}(\partial_t-\beta^k\partial_k)\sqrt{h}=-\sqrt{h}K+\frac{1}{\alpha}\sqrt{h}\,\partial_k\beta^k \ . \tag{2.22}$$

To have a complete set of evolution equations we need to specify equations for the lapse α and the shift β^i, i.e., to choose a gauge. The simplest choice is the synchronous gauge

$$\alpha\equiv1 \ , \qquad \beta^i\equiv0 \ . \tag{2.23}$$

Another choice particularly straightforward to implement in this context is the harmonic gauge

$$\frac{1}{\alpha}(\partial_t-\beta^k\partial_k)\alpha=-\alpha K \ , \tag{2.24}$$

$$\frac{1}{\alpha}(\partial_t-\beta^k\partial_k)\beta^i=-\alpha\left[h^{ij}\frac{\partial_j\alpha}{\alpha}+\frac{1}{\sqrt{h}}\partial_j(\sqrt{h}\,h^{ij})\right] \ . \tag{2.25}$$

The evolution equations, Eqs. (2.7), (2.8), (2.17), (2.18), (2.20), and (2.22), are valid for any gauge and we will retain this property as we code them. We do not attempt to simplify them by choosing a particular gauge.

We code these evolution equations in conservative form. The conservative form of Eq. (2.22) is

$$\partial_t\sqrt{h}-\partial_k(\beta^k\sqrt{h})=-\alpha\sqrt{h}K \ . \tag{2.26}$$

From this follows a general conversion rule: If the original form is

$$(\partial_t-\beta^k\partial_k)f=g \ , \tag{2.27}$$

then the conservative form is

$$\partial_t\tilde{f}-\partial_k(\beta^k\tilde{f})=\tilde{g}-\alpha K\tilde{f} \ , \tag{2.28}$$

where

$$\tilde{f}\equiv\sqrt{h}f \ , \tag{2.29}$$

etc.

Our final set of equations is

$$\partial_t\tilde{K}-\partial_k(\beta^k\tilde{K})=-\partial_i(\tilde{h}^{ij}\partial_j\alpha)+\alpha\sqrt{h}R-8\pi G\alpha\tilde{h}^{ij}\partial_i\phi\,\partial_j\phi-24\pi G\alpha\sqrt{h}V(\phi) \ , \tag{2.30}$$

$$\partial_t\tilde{A}^i_j-\partial_k(\beta^k\tilde{A}^i_j)=-\tilde{h}^{ik}(\partial_j\partial_k\alpha-\Gamma^l_{jk}\partial_l\alpha)+\alpha\tilde{h}^{ik}R_{kj}-8\pi G\alpha\tilde{h}^{ik}\partial_k\phi\,\partial_j\phi -\tfrac{1}{3}\delta^i_j[-\partial_k(\tilde{h}^{kl}\partial_l\alpha)+\alpha\sqrt{h}R-8\pi G\alpha\tilde{h}^{kl}\partial_k\phi\partial_l\phi]+\partial_j\beta^k\tilde{A}^i_k-\partial_k\beta^i\tilde{A}^k_j \ , \tag{2.31}$$

$$\partial_t\tilde{\eta}-\partial_k(\beta^k\tilde{\eta})=\partial_i(\alpha\tilde{h}^{ij}\partial_j\phi)-\alpha\sqrt{h}\,V'(\phi)\ , \tag{2.32}$$

$$\partial_t\sqrt{h}\,-\partial_k(\beta^k\sqrt{h}\,)=-\alpha\sqrt{h}\,K\ , \tag{2.33}$$

$$\partial_t\tilde{h}_{ij}-\partial_k(\beta^k\tilde{h}_{ij})=-\tfrac{5}{3}\alpha K\tilde{h}_{ij}-2\alpha A_j^l\tilde{h}_{il}+\partial_j\beta^l\tilde{h}_{il}+\partial_i\beta^l\tilde{h}_{lj}\ , \tag{2.34}$$

$$\partial_t\tilde{\phi}-\partial_k(\beta^k\tilde{\phi})=-\alpha K\tilde{\phi}+\alpha\tilde{\eta}\ . \tag{2.35}$$

The harmonic gauge equations in conservative form are

$$\partial_t\tilde{\omega}-\partial_k(\beta^k\tilde{\omega})=0\ , \tag{2.36}$$

$$\partial_t\tilde{\beta}^i-\partial_k(\beta^k\tilde{\beta}^i)=-\alpha K\tilde{\beta}^i-\alpha^2\left[\tilde{h}^{ij}\frac{\partial_j\alpha}{\alpha}+\partial_j\tilde{h}^{ij}\right]\ , \tag{2.37}$$

where $\omega\equiv 1/\alpha$, or $\tilde{\omega}\equiv\sqrt{h}\,/\alpha$.

We need initial data that satisfies the constraint equations (2.9) and (2.10), which we can write as

$$R+\tfrac{2}{3}K^2-A_j^iA_i^j=8\pi G[h^{ij}\partial_i\phi\,\partial_j\phi+\eta^2+2V(\phi)]\ , \tag{2.38}$$

$$\partial_iA_j^i+\Gamma_{li}^iA_j^l-\Gamma_{ji}^lA_l^i-\tfrac{2}{3}\partial_jK=-8\pi G\eta\partial_j\phi\ . \tag{2.39}$$

We discussed the procedure for solving the initial value problem in Ref. [8]. In addition to these numerically solved initial data, we have also used data that satisfies the constraints trivially.

This latter method, previously used by Goldwirth and Piran [6], involves two scalar fields to achieve a momentarily flat space for the initial slice. One of the scalar fields is the inflaton field ϕ which can be set arbitrarily according to the problem we wish to solve. The other field, ϕ_R, is an auxiliary field, with $V(\phi_R)\equiv 0$. We want the right-hand side of Eq. (2.38) to be constant, and that of Eq. (2.39) to be zero on the initial slice. This is achieved by setting

$$\begin{aligned}&\eta\equiv 0\ ,\\ &\phi_R\equiv 0\ ,\\ &\eta_R\equiv[2\rho_H-h^{ij}\partial_i\phi\,\partial_j\phi-2V(\phi)]^{1/2}\ ,\end{aligned} \tag{2.40}$$

where $\rho_H=$const. Equations (2.38) and (2.39) can now be satisfied with

$$\begin{aligned}&K\equiv-3\left[\frac{8\pi G\rho_H}{3}\right]^{1/2}\ ,\\ &A_j^i\equiv 0\ ,\\ &h_{ij}\equiv\delta_j^i\ .\end{aligned} \tag{2.41}$$

The initial slice will thus have a homogeneous total energy density, but with an inhomogeneous composition. The energy density becomes inhomogeneous immediately when it is evolved. In a typical run, ϕ_R soon redshifts away whereas the vacuum energy $V(\phi)$ keeps the inflaton field dynamically important.

III. NUMERICAL TECHNIQUES

Replacing the continuous spacetime with a discrete grid requires a decision about the relative positioning of variables on the grid. As discussed below, we have divided the variables into two sets staggered in time. This division arises naturally from the form of the equations, although some terms in the equations violate this structure and require interpolation.

In the previous section, Eqs. (2.30)–(2.35) are written in the order they are actually evolved in our code. The lapse is calculated before $\sqrt{h}$, and the shift before $\tilde{K}$. This ordering is determined by what quantities are needed to evolve which quantity. The quantities α, $\sqrt{h}$, $\tilde{h}_{ij}$, and $\tilde{\phi}$ are evaluated after the full time step, i.e., at times

$$t^{n-1},t^n\equiv t^{n-1}+\Delta t^n,\ldots,$$

where Δt^n is the nth time step. The quantities β^i, $\tilde{K}$, $\tilde{A}_j^i$, and $\tilde{\eta}$ are evaluated at half-time, i.e., at times

$$t^{n-1}+\tfrac{1}{2}\Delta t^n,t^n+\tfrac{1}{2}\Delta t^{n+1},\ldots\ .$$

With the possible exception of lapse and shift, this scheme does not require any extrapolation in time. All quantities that are needed to evolve a particular quantity have already been evolved to the time level at which they are needed. The quantities α, β^i, $\sqrt{h}$, and K are needed at both full and half-time, so they are interpolated when needed. Depending on the choice of gauge, the calculation of α and β^i at a new time level may require extrapolation of some quantities in time, and should then be iterated.

It is a common practice to have a similar staggering in space. A gradient of a variable would naturally lie between the grid points where the variable is located. In a three-dimensional (3D) code this becomes complicated. Picture the grid dividing the space into small cubes, or zones. Some variables might naturally lie at zone centers, others at zone faces, and yet others at zone edges. The grid will have 3 times as many faces and edges as zones (in three different orientations). Typically the different components of a three-vector would lie on differently oriented faces. If the equations respect such a structure, the extra coding effort will pay off by giving a good accuracy with a small number of zones. We, however, did not find our equations to naturally fit into such a scheme. Because so many terms would have to be interpolated, it appeared unlikely that this would lead to much improved performance. Therefore, we decided to position all the variables the same way in space. We refer to these locations simply as grid points. To obtain a value of a spatial derivative at a grid point we thus need to difference over two grid spacings.

For simplicity and generality, we are using Cartesian coordinates. We have coded for nonuniform grid spacings in x, y, and z. However, to maintain second-order accuracy in space with a nonuniform grid the spacing

should not vary too steeply. A variable will lie at a grid-point (x,y,z), where, e.g., x takes on any of the values $x_1,\ldots,x_{N_x}$, and

$$x_n = x_{n-1} + \Delta x_n \ . \tag{3.1}$$

The first and last grid points in each direction, e.g., at x_1 and x_{N_x}, are dummies. Variables are not evolved at these grid points but are set after the evolution according to the boundary condition. Thus the "physical" grid has only $(N_x-2)(N_y-2)(N_z-2)$ points.

Periodic boundary conditions are

$$\begin{aligned} f(x_{N_x},y,z) &= f(x_2,y,z) \ , \\ f(x_1,y,z) &= f(x_{N_x-1},y,z) \ , \end{aligned} \tag{3.2}$$

etc. Reflective boundary conditions for tensors are different than for scalars, because some components change signs, e.g.,

$$\begin{aligned} \beta^1(x_1,y,z) &= -\beta^1(x_2,y,z) \ , \\ h_{12}(x_1,y,z) &= -h_{12}(x_2,y,z) \ . \end{aligned} \tag{3.3}$$

The largest piece of the evolution code is the calculation of the Ricci tensor R_{ij}. It is calculated from the three-metric h_{ij} and is needed for evolving the extrinsic curvature. In the process we obtain the connection coefficients Γ^i_{jk}, also needed for evolving A^i_j. (Γ^i_{jk} is also needed for checking the momentum constraint, and $R \equiv R^i_i$ is needed for checking the Hamiltonian constraint.) These are computed directly from their definitions

$$\Gamma^i_{jk} \equiv \tfrac{1}{2} h^{il}(\partial_k h_{lj} + \partial_j h_{lk} - \partial_l h_{jk}) \tag{3.4}$$

and

$$\begin{aligned} R_{ij} &\equiv \partial_k \Gamma^k_{ij} - \partial_j \Gamma^k_{ik} + \Gamma^k_{lk}\Gamma^l_{ij} - \Gamma^k_{lj}\Gamma^l_{ik} \\ &= \tfrac{1}{2}\partial_k h^{kl}(\partial_j h_{li} + \partial_i h_{lj} - \partial_l h_{ij}) + \tfrac{1}{2} h^{kl}(\partial_k \partial_j h_{li} + \partial_k \partial_i h_{lj} - \partial_k \partial_l h_{ij}) - \tfrac{1}{2}\partial_j h^{kl}\partial_i h_{lk} - \tfrac{1}{2} h^{kl}\partial_j \partial_i h_{lk} + \Gamma^k_{lk}\Gamma^l_{ij} - \Gamma^k_{lj}\Gamma^l_{ik} \ . \end{aligned} \tag{3.5}$$

(We first invert h_{ij} to obtain h^{ij}.) We use the latter form for R_{ij} to avoid taking derivatives of Γ^i_{jk}, which already involves derivatives. With our grid structure we obtain second derivatives more compactly by calculating them directly.

There are 6 components of R_{ij} and 18 components of Γ^i_{jk} to be calculated, with double sums. This could have been coded with loops over the indices, relying on the compiler to unroll the summation loops to permit vectorizing. However, there are complications due to the symmetries in indices. Also, many of the terms cancel out with certain combinations of indices. Therefore, we have coded in all components separately, with the sums written out. We actually wrote a small program to produce this long (almost 600 lines of FORTRAN) but repetitive piece of code.

The evolution equations are mostly rather straightforward to code. Since we are evolving the quantities with carets [see Eq. (2.29)] which are often needed without carets, we have to be careful to multiply and divide by $\sqrt{h}$ when needed. To make this possible, $\sqrt{h}$ has to be evolved to a new full-time level first.

The present version of the code does not yet include the advection terms $\partial_k(\beta^k f)$, and is therefore restricted to $\beta^i \equiv 0$. Also, the right-hand-side terms involving β^i have been left out in the $\tilde{A}^i_j$ and $\tilde{h}_{ij}$ equations. This allows us to evolve $\tilde{A}^i_j$ without matrix inversion.

The evolution of $\tilde{h}_{ij}$ involves matrix inversion since the right-hand side of Eq. (2.34) contains other components of this tensor in the $-2\alpha A^l_j \tilde{h}_{il}$ term. With $\beta^i \equiv 0$, the discretized form of this equation (taking us from t^n to t^{n+1}) can be written as

$$H^{n+1} = H^n - \tfrac{1}{2}\alpha\Delta t M(H^n + H^{n+1}) \tag{3.6}$$

or

$$H^{n+1} = (1+\tfrac{1}{2}\alpha\Delta t M)^{-1}(1-\tfrac{1}{2}\alpha\Delta t M)H^n \ , \tag{3.7}$$

where $H \equiv (\tilde{h}_{11},\tilde{h}_{12},\tilde{h}_{13},\tilde{h}_{22},\tilde{h}_{23},\tilde{h}_{33})$ is a six-component vector, and M is a 6×6 matrix, whose components are linear combinations of the extrinsic curvature components. A matrix inversion at each grid point would be rather time consuming. As we only need second-order accuracy in Δt, we replace Eq. (3.7) by

$$H^{n+1} = (1-\alpha\Delta t M + \tfrac{1}{2}\alpha^2\Delta t^2 M^2)H^n \ , \tag{3.8}$$

which requires mere matrix multiplication, and does not prevent vectorization over the grid.

A similar procedure will have to be utilized in the evolution of $\tilde{A}^i_j$ once nonzero shift is included. Presently, we evolve each component separately. Although only five of the components are independent, we evolve all nine of them since reconstructing the remaining components from the minimum set of five is nontrivial. (Since $\tilde{A}^i_i = 0$, we could easily skip evolving one of the diagonal components.) The covariant components are symmetric, so if we rewrote Eq. (2.31) to evolve $\tilde{A}_{ij}$ instead of $\tilde{A}^i_j$, there would be only six components to evolve. But this gives a nonlinear equation, whereas Eq. (2.31) is linear in $\tilde{A}^i_j$.

We are presently running free evolution; i.e., the constraint equations are not solved after the initial slice. To see how accurately the constraints are maintained, we compare the left- and right-hand sides of Eqs. (2.38) and (2.39) during the evolution.

We use three conditions to determine the time step. The first is the Courant condition. The code requires three time steps to carry information from the grid point (x_l, y_m, z_n) diagonally to $(x_{l+1}, y_{m+1}, z_{n+1})$. The time step must be short enough that this grid velocity is not less than the speed of light. To satisfy this condition everywhere, we need to find the shortest physical distance Δs, where

$$\Delta s^2 = h_{ij} \Delta x^i \Delta x^j , \tag{3.9}$$

between neighboring points. To be more precise, we set

$$\Delta t_C = C \min(\Delta s / \alpha d) , \tag{3.10}$$

where $d = 1$, 2, or 3 depending on whether the neighboring point differs in one, two, or three coordinates, and $C < 1$. In practice, we have used $C = 0.7$.

The second condition is an expansion condition. According to Eq. (2.33), the local volume expansion rate is given by $-\alpha K$. To keep expansion per time step below a certain amount E, we set

$$\Delta t_E = E / \max(\alpha |K|) . \tag{3.11}$$

The third condition is a smoothness condition. To prevent the time step from increasing too rapidly, we set

$$\Delta t_S = (1+S) \Delta t_{\text{previous}} . \tag{3.12}$$

The time step is then the smallest of these three:

$$\Delta t = \min(\Delta t_C, \Delta t_E, \Delta t_S) . \tag{3.13}$$

The Courant condition gives a shorter time step when the number of grid points is increased. In the runs presented here, we adjusted the other two conditions with grid size so that halving the grid spacing also halved the time step consistently over the whole run. Thus we have used $E = 0.1(32/N)$ and $S = 0.01(32/N)$, where N is the number of grid points in one direction.

In practice, the controlling condition was the Courant condition in the early part of the run, the expansion condition during most of the inflation, and the smoothness condition after inflation. The time scale of the postinflation oscillations of ϕ is not related to any of these three conditions. Indeed, when we ran long enough, the time step became too long to resolve these oscillations. We experimented with a fourth condition to control this, but could not easily find one that is both general and simple. Instead, we just chose a small enough value for S to resolve the first oscillations, as we were not interested in the later ones. In running different problems it may be useful to experiment with the time-step control, to optimize it for each case.

IV. CODE TESTS

A. Homogeneous tests

The simplest test is a homogeneous one. We did a homogeneous chaotic inflation [10] run with the potential $V(\phi) = \frac{1}{4}\lambda\phi^4$, $\lambda = 10^{-3}$, and the inflaton field initially at $\phi = 5 m_{\text{Pl}}$. The perturbation runs below are perturbations around this homogeneous run. Figures 1 and 2 show the time evolution of the inflaton ϕ and the scale factor a, respectively. The code deviates from the exact results by less than 10^{-3}. Another run with a different time step showed the error to be quadratic in time step. We also ran a Kasner model, where the expansion rates along the three axes were all different, and obtained similar accuracy.

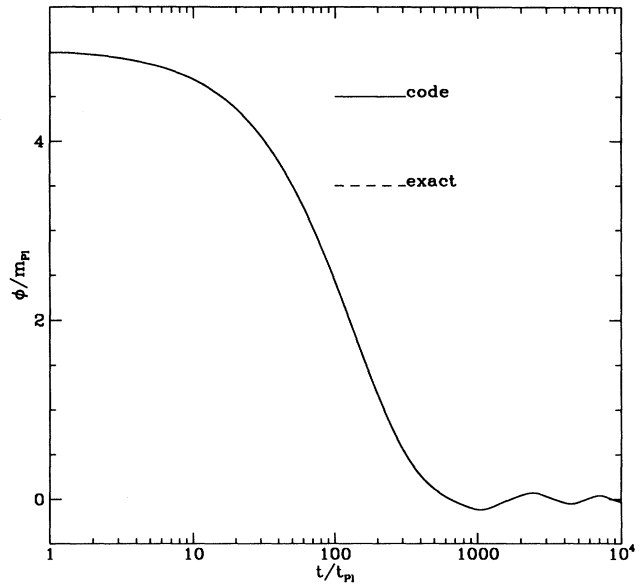

FIG. 1. The inflaton field ϕ as a function of time in homogeneous chaotic inflation. The lines showing the code result and the exact result fall on top of each other and cannot be distinguished by eye. Inflation ends near $t = 300 t_{\text{Pl}}$.

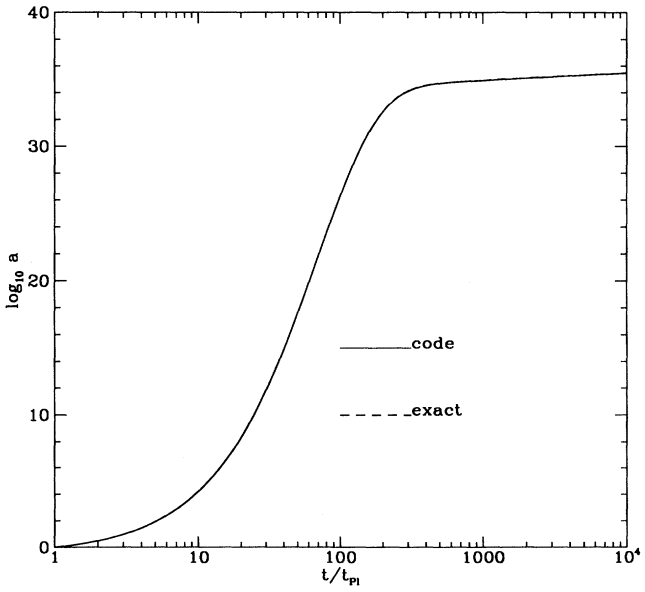

FIG. 2. Same as Fig. 1, but for the scale factor a. Inflation ends after a linear expansion of 10^{34}, or a volume expansion of 10^{102}.

B. Perturbation tests

The perturbation theory for inflation has been discussed by Brandenberger, Kahn, and Press [11]. The unperturbed spacetime is assumed to be spatially flat. We shall work in the synchronous gauge. The metric and the inflaton field can be written as

$$ds^2=-dt^2=a(t)^2\{[1+A(t,\mathbf{x})]\delta_{ij}+B(t,\mathbf{x})_{,ij}\}dx^i dx^j \tag{4.1}$$

and

$$\phi(t,\mathbf{x})=\phi_0(t)+\delta\phi(t,\mathbf{x}) , \tag{4.2}$$

where $\delta\phi$, A, and B are small perturbations. The zeroth order, or homogeneous, equations are

$$H^2\equiv\left[\frac{\dot a}{a}\right]^2=\frac{8\pi G}{3}\left[\frac{1}{2}\dot\phi_0^2+V(\phi_0)\right] , \tag{4.3}$$

$$2\frac{\ddot a}{a}+\left[\frac{\dot a}{a}\right]^2=-8\pi G\left[\frac{1}{2}\dot\phi_0^2-V(\phi_0)\right] , \tag{4.4}$$

and

$$\ddot\phi_0+3H\dot\phi_0+V'(\phi_0)=0 , \tag{4.5}$$

where Eq. (4.3) is the Hamiltonian constant. The momentum constraint vanishes identically to zeroth order.

We expand the perturbations in plane waves

$$\delta\phi(t,\mathbf{x})=\sum_k \delta\phi_k(t)e^{i\mathbf{k}\cdot\mathbf{x}} , \tag{4.6}$$

etc., where $\mathbf{k}$ is the comoving wave vector. The first-order perturbation equations for the modes $\delta\phi_k(t)$, $A_k(t)$, and $B_k(t)$ are then

$$3\ddot A_k-k^2\ddot B_k+3H(3\dot A_k-k^2\dot B_k)+k^2a^{-2}A_k =-24\pi G[\dot\phi_0\delta\dot\phi_k-V'(\phi_0)\delta\phi_k] , \tag{4.7}$$

$$\ddot A_k+3H\dot A_k=-8\pi G[\dot\phi_0\delta\dot\phi_k-V'(\phi_0)\delta\phi_k] , \tag{4.8}$$

$$-k^2a^{-2}A_k-H(3\dot A_k-k^2\dot B_k) =-8\pi G[\dot\phi_0\delta\dot\phi_k+V'(\phi_0)\delta\phi_k] , \tag{4.9}$$

$$\dot A_k=-8\pi G\dot\phi_0\delta\phi_k , \tag{4.10}$$

$$\delta\ddot\phi_k+3H\delta\dot\phi_k+V''(\phi_0)\delta\phi_k =-k^2a^{-2}\phi_k-\tfrac{1}{2}\dot\phi_0(3\dot A_k-k^2\dot B_k) . \tag{4.11}$$

To obtain "exact" perturbation theory results, we solved these ordinary differential equations with the Runge-Kutta method. The metric evolution equations (4.4), (4.7), and (4.8) can here be ignored, and the metric (a, A_k, B_k) can be evolved using the constraint equations (4.3), (4.9), and (4.10).

For the perturbation runs with the code, we need the relation between the code variables K and A^i_j, and the perturbation theory variables A and B. From the metric evolution equation (2.12) we obtain

$$K_0=-3H , \tag{4.12}$$

$$\delta K=-\tfrac{3}{2}\dot A-\tfrac{1}{2}\nabla^2\dot B , \tag{4.13}$$

$$A^i_j=-\tfrac{1}{2}\dot B_{,ij}+\tfrac{1}{6}\delta_{ij}\nabla^2\dot B , \tag{4.14}$$

with $K=K_0+\delta K$. The scalar three-curvature is

$$R=-2a^{-2}\nabla^2 A . \tag{4.15}$$

The initial data has to satisfy the perturbation theory constraint equations (4.9) and (4.10). This is accomplished by choosing arbitrary values for ϕ_0, $\dot\phi_0$, $\delta\phi$, $\delta\dot\phi$, A, and B, and solving for $\dot A$ and $\dot B$ from Eqs. (4.9) and (4.10). For our test runs we have chosen initial data of the form

$$\begin{aligned} &a=1 ,\\ &\phi_0=5m_{\rm Pl} ,\\ &\dot\phi_0=0 ,\\ &\delta\phi=\sum_k \delta\phi_k e^{i\mathbf{k}\cdot\mathbf{x}} ,\\ &\delta\dot\phi=0 ,\\ &A=0 ,\\ &B=0 . \end{aligned} \tag{4.16}$$

For this case, the constraint equations (4.9) and (4.10) give

$$\begin{aligned} &\dot A_k=0 ,\\ &\dot B_k=-\frac{8\pi G}{Hk^2}V'(\phi_0)\delta\phi_k . \end{aligned} \tag{4.17}$$

The initial values for the extrinsic curvature variables are thus

$$\begin{aligned} &K_0=-3H ,\\ &\delta K=-4\pi G\frac{V'(\phi_0)}{H}\sum_k \delta\phi_k e^{i\mathbf{k}\cdot\mathbf{x}} ,\\ &A^i_j=\frac{4\pi G}{H}V'(\phi_0)\sum_k\left[\frac{1}{3}\delta_{ij}-\frac{k_ik_j}{k^2}\right]\delta\phi_k e^{i\mathbf{k}\cdot\mathbf{x}} , \end{aligned} \tag{4.18}$$

where

$$H=\left[\frac{8\pi G}{3}V(\phi_0)\right]^{1/2} . \tag{4.19}$$

The particular initial data we have used are a superposition of three perpendicular plane waves,

$$\delta\phi(t_0,\mathbf{x})=\delta\phi_1(t_0)e^{ik_1x}+\delta\phi_2(t_0)e^{ik_2y} +\delta\phi_3(t_0)e^{ik_3z} , \tag{4.20}$$

with small and equal amplitudes

$$\delta\phi_1(t_0)=\delta\phi_2(t_0)=\delta\phi_3(t_0)=10^{-6} , \tag{4.21}$$

but different wavelengths $L_i=2\pi/k_i$,

$$L_1=0.2H^{-1} , \quad L_2=0.3H^{-1} , \quad L_3=0.4H^{-1} . \tag{4.22}$$

Here the subscripts $i=1,2,3$ denote the three different modes, rather than components of a vector. Our grid had one wavelength in each direction. To get the same number $N_x=N_y=N_z$ or grid points per each wavelength, we have used different grid spacings Δx^i in each direction.

We studied the convergence of the code results towards the perturbation theory results as the number of grid points is increased (the time step and grid spacing is decreased). The results are shown in Figs. 3–5. These show

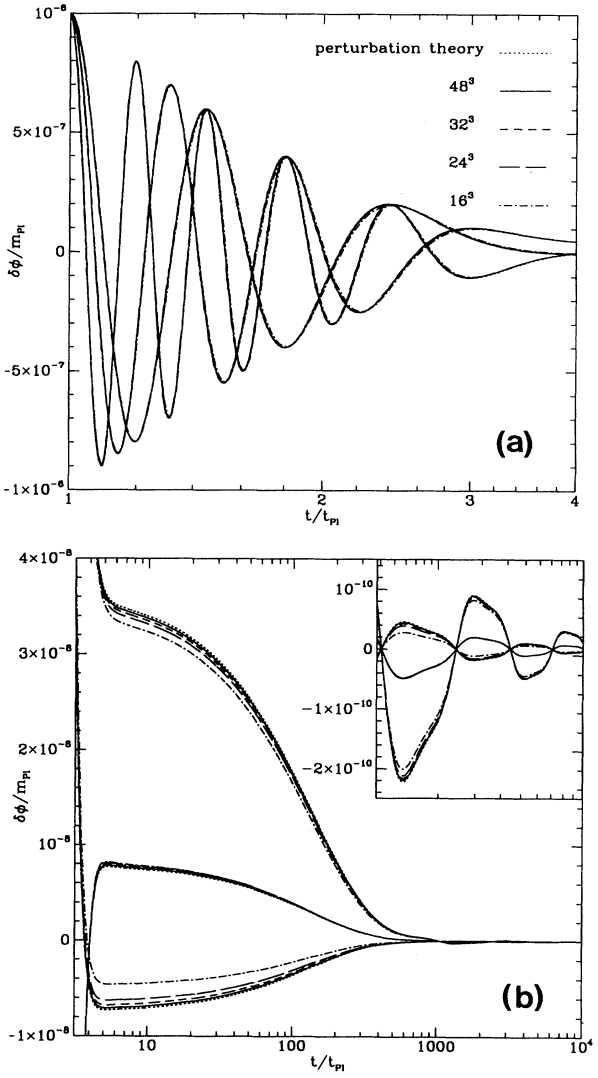

FIG. 3. The amplitudes of the three perpendicular plane-wave perturbations $\delta\phi_1$, $\delta\phi_2$, and $\delta\phi_3$ in the inflaton field. The different line styles show code results with different grid resolutions, as well as the perturbation theory result. (a) Early part of the run, perturbations inside the horizon. The perturbations with the longer wavelengths have longer oscillation periods, but all are damped by the expansion at the same rate. In this case the code results are rather accurate, and the lines fall onto each other. (b) Late part of the run, perturbations outside the horizon: The vertical scale has been expanded by a factor of 25. The inset displays the last decade (from $t=10^3 t_{\rm Pl}$ to $t=10^4 t_{\rm Pl}$) with a further expanded scale to show the postinflation oscillations.

the evolution of the amplitude of the three perpendicular perturbation waves in ϕ, A, and B.

Initially, the waves are well inside the horizon. (By "horizon" we refer to the Hubble length, as is common among astroparticle physicists.) The Hubble constant at the initial time is

$$H=\left[\frac{8\pi\lambda}{3m_{\rm Pl}^2}\right]^{1/2}\left[\frac{\phi_0}{m_{\rm Pl}}\right]^2=2.29m_{\rm Pl}\ . \tag{4.23}$$

The initial values of k_i/H were 10π, $20\pi/3$, and 5π. We have arbitrarily set the initial time as $t_0=t_{\rm Pl}$. As the Universe inflates, the waves exit the horizon one by one. Defining the time of exit by $k_i=H$, this happens at

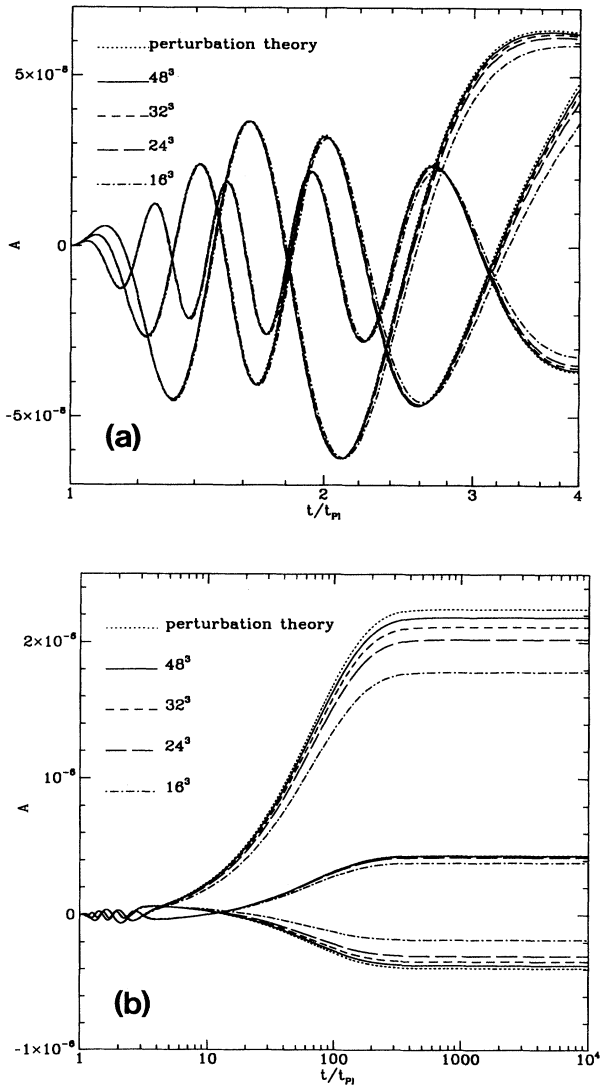

FIG. 4. Same as Fig. 3, but for the perturbations A_1, A_2, and A_3 in the metric. (a) Early part of the run. (b) The entire run. The perturbations exit the horizon between $t=2t_{\rm Pl}$ and $3t_{\rm Pl}$ and the oscillatory behavior changes to monotonic growth, which ceases as inflation ends.

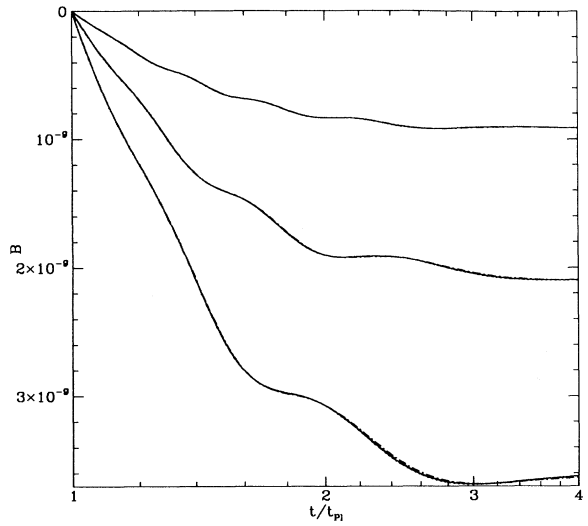

FIG. 5. Same as Fig. 3, but for the perturbations B_1, B_2, and B_3 in the metric. We only show the early part of the run, because in the late part B stays almost constant in time.

$t=2.20t_{\rm Pl}$, $2.33t_{\rm Pl}$, and $2.51t_{\rm Pl}$.

The behavior of the perturbations change markedly as they exit the horizon. Inside the horizon, the initial ϕ perturbation oscillates and these oscillations are damped by the expansion, all three wavelengths at the same rate. There was no initial perturbation A, or B, in the metric, but these are now induced by the ϕ perturbation. The A perturbation oscillates with a growing amplitude, a quarter phase behind $\delta\phi$. The B perturbation exhibits monotonic growth with a small oscillation superimposed. The metric perturbations do not have time to reach the ϕ perturbation amplitude before the perturbations exit the horizon.

Outside the horizon the oscillations cease. The ϕ perturbation decreases while A grows and B stays constant. At the end of inflation the growth in A ceases, whereas $\delta\phi$ shows anharmonic oscillation with ϕ_0 around the bottom of $V(\phi)$.

The discretization error exhibits a quadratic behavior when we increase the number of grid points from 16^3 to 48^3. The errors in B are small, as are the errors in A and $\delta\phi$ while inside horizon. The larger errors in $\delta\phi$ and A outside the horizon are due to the switch from oscillating to monotonic behavior, when a small phase error leads to a relatively large amplitude error. Even then, the errors in the final values in the 48^3 runs are less than 3%, after a volume expansion by more than 10^{100}.

C. Memory and time requirements

The code has 56 variables per grid point. These are $\sqrt{h}$, h_{ij} (6), h^{ij} (6), Γ^i_{jk} (18), R_{ij} (6), R, α, β^i (3), K, A^i_j (9), ϕ, η, ϕ_R, and η_R (the numbers in parentheses indicate the number of component variables). In addition, 30 memory locations per grid point are used for work space or auxiliary variables. The code is not optimized for memory usage but rather for simplicity, so memory savings could be achieved at the cost of making the code more complicated, less readable and more time-consuming. Thus the code requires 86 words of memory per grid point, or about 24 Mwords for a 64^3 run. In practice, the largest grid that fit in the 32M queue on the Cray-2 at NCSA was 70^3.

The code runs at 140 Mflops on a single processor, and takes about 0.02 ms of computation time per grid point and cycle. Thus a 64^3 grid runs at about 700 cycles per hour. To run the 70 e-foldings of inflation required to obtain the observable Universe from one preinflation Hubble volume takes almost 10 h of Cray time with this resolution. The most time is spent on calculating the connection coefficients Γ^i_{jk} and the Ricci tensor R_{ij}, about 43% of total time. The second most time is used in the evolution of the extrinsic curvature tensor A^i_j, 11%.

V. INHOMOGENEOUS INFLATION RUNS

We now present some runs of inhomogeneous inflation. These 64^3 runs use the flat initial data described in Sec. II. A run using initial data obtained with the initial data solver was presented in Ref. [12].

The requirement that the initial time slice has homogeneous total energy density (as implied by flat initial data) gives an upper limit for the variation of the inflaton field ϕ within a Hubble length. From

$$\frac{1}{2}(\nabla\phi)^2<\rho=\frac{3m_{\rm Pl}^2}{8\pi}H^2 \tag{5.1}$$

we get

$$\nabla\phi<\left[\frac{3}{4\pi}\right]^{1/2}\frac{m_{\rm Pl}}{H^{-1}}\ . \tag{5.2}$$

Thus inhomogeneities that begin inside the horizon have small amplitudes. Runs where we had large initial variation in the inflaton field have initial grid lengths L equal to many Hubble lengths.

These runs are of chaotic inflation. The potential is $V(\phi)=\frac{1}{4}\lambda\phi^4$, with $\lambda=10^{-6}$. We chose initial data of the form

$$\phi(t_0,\mathbf{x})=\phi_0+\delta\phi\sum_{l,m,n=1}^{2}\frac{1}{lmn}\sin x_l\sin y_m\sin z_n\ , \tag{5.3}$$

where $x_l=2\pi lx/L+\theta_{xl}$, etc., with θ_{xl} random phases. The initial Hubble constant was chosen to be $H=0.1m_{\rm Pl}$, and $\phi_0=5m_{\rm Pl}$.

We present a small-scale run with $L=H^{-1}$, $\delta\phi=0.0125m_{\rm Pl}$, and a large-scale run with $L=32H^{-1}$, $\delta\phi=0.4m_{\rm Pl}$. The phases for these particular runs were $\theta_{x1}=3.83$, $\theta_{x2}=2.59$, $\theta_{y1}=3.02$, $\theta_{y2}=1.83$, $\theta_{z1}=3.19$, and $\theta_{x2}=1.33$. The same phases were used in both runs. In the initial data, the minimum ϕ value turned out to be $\phi_0-3.3\delta\phi$, and the maximum $\phi_0+2.1\delta\phi$. The maximum value of $\nabla\phi$ was within a factor of 2 from the upper limit. In Fig. 6 we show the regions of small and large ϕ.

The results are shown as three-dimensional contour plots of the scalar variables ϕ, $\sqrt{h}$, K, and R. These are supplemented by one-dimensional plots showing the

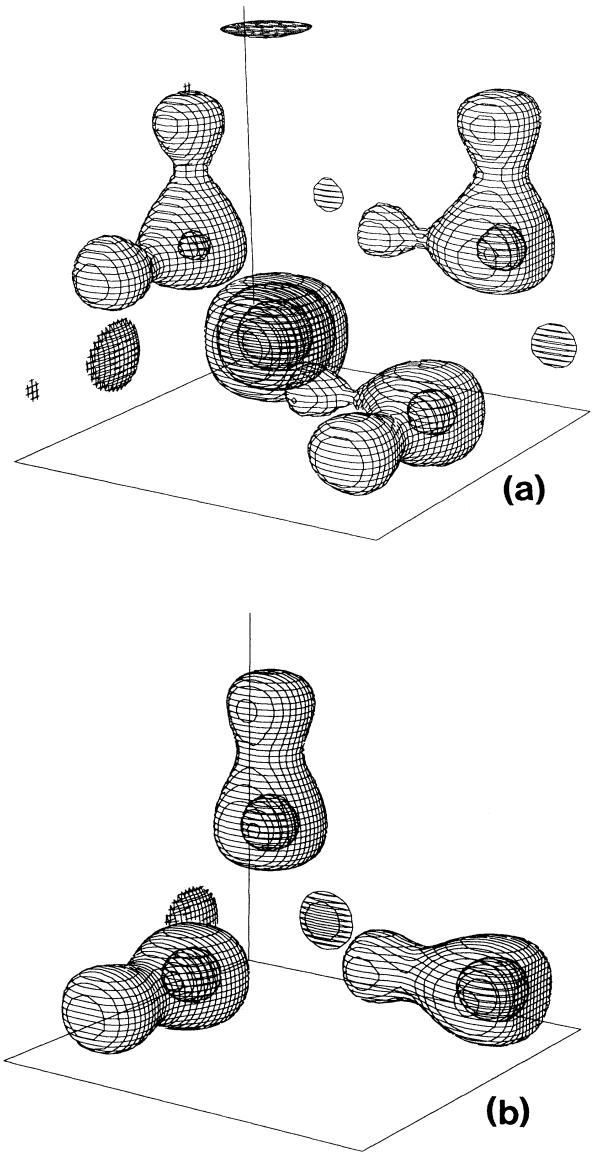

FIG. 6. Regions of small and large values of ϕ in the initial data. We express the contour levels as a percentage between the minimum (0%) and the maximum (100%) value in the slice. (a) The regions of small ϕ are enclosed by 20%, 40%, and 50% contours. In the small-scale run these correspond to $\phi=4.973m_{\rm Pl}$, $4.986m_{\rm Pl}$, and $4.993m_{\rm Pl}$. In the large-scale run the contours have $\phi=4.12m_{\rm Pl}$, $4.55m_{\rm Pl}$, and $4.77m_{\rm Pl}$. The minimum value, near the back corner enclosed by all three contours, was $4.959m_{\rm Pl}$ in the small-scale run, and $3.69m_{\rm Pl}$ in the large-scale run. (b) The regions of large ϕ are shown enclosed by 75% and 90% contours ($5.010m_{\rm Pl}$ and $5.020m_{\rm Pl}$ for the small-scale run, $5.31m_{\rm Pl}$ and $5.63m_{\rm Pl}$ for the large-scale run). The maximum value was $5.026m_{\rm Pl}$ in the small-scale run, and $5.85m_{\rm Pl}$ in the large-scale run. In some of the following figures, quantities are plotted along a reference line. This line runs parallel to the y axis, which in this figure goes to the right from the origin. The reference line goes through the initial ϕ minimum near the back corner and through the region with large ϕ near the right end of the y axis.

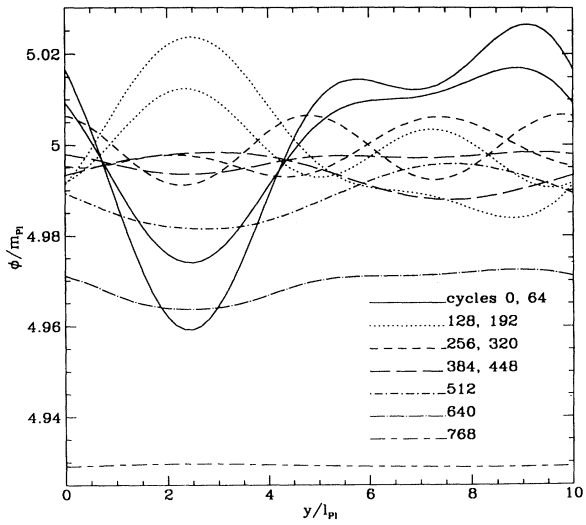

FIG. 7. Figures 7–14 show results from the small-scale run. This figure shows the inflaton field along the reference line at various time slices. These correspond to $t/t_{\rm Pl}=5$ (initial time), 5.6, 6.4, 7.6, 9.2, 11.3, 14.3, 18.5, 24.1, 42.6, and 77.7. The Hubble time was initially $10t_{\rm Pl}$. At the last slice shown, where inflation has taken hold, the potential contributing 99.6% of total energy, the approximate Hubble time is $28t_{\rm Pl}$.

quantities along a reference line at different time slices. This reference line runs parallel to the y axis and goes through the initial ϕ minimum. Figure 6 applies to the initial data of both the small- and the large-scale runs, although the *amplitude* of these ϕ variations were of different magnitude.

We discuss the small-scale run first. The grid length was initially set equal to one Hubble length. Thus the inhomogeneities are at first well inside the horizon. The

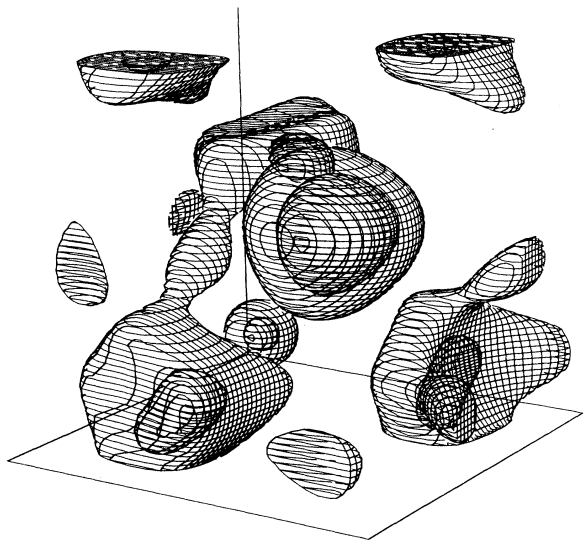

FIG. 8. The inflaton field at $t=9.2t_{\rm Pl}$. We show regions of small ϕ enclosed by 15% and 30% contours.

dynamical time scale of the inflaton field is therefore shorter than the expansion time scale, given by the Hubble time. At the initial slice the energy density is dominated by the kinetic energy of the ϕ and ϕ_R fields, accounting for 84% of total energy. 13% of the energy is in $V(\phi)$ and 3% in field gradients (although at the point of maximum $\nabla\phi$ they account for more than half of the energy density). The initial Hubble time is $t_H = 10t_{\rm Pl}$. We arbitrarily set the initial time as $t_0 = t_H(t_0)/2 = 5t_{\rm Pl}$. The time step is at first controlled by the Courant condition, and thus we get several hundred time steps per Hubble time. We show a number of contour plots of the slice at cycle 256, or $t = 9.2t_{\rm Pl}$. Of the total energy in this slice, 52% is kinetic, 46% potential, and 2% gradient. The Hubble time is now roughly $18t_{\rm Pl}$, so this slice is about a quarter of a Hubble time from the beginning.

As the inhomogeneities evolve, they oscillate and their amplitude is damped (see Fig. 7). After a quarter of a Hubble time of evolution, the regions of small and large ϕ are quite different from what they were initially (see Fig. 8). By the time the inhomogeneities have exited the horizon, the inflaton field has become much more homogeneous than it was initially.

Since we started with flat initial data, $\sqrt{h}$, K, and R were all homogeneous at the initial time (and R was zero). The inhomogeneities in ϕ induce inhomogeneities in these curvature quantities.

We show regions of small and large expansion $\sqrt{h}$ after a quarter of a Hubble time in Fig. 9. Regions of both large and small initial ϕ end up as regions of small expansion. The region of largest expansion forms a shell surrounding the initial ϕ minimum. This is partly due to the large gradient energies in this region at early times, and partly due to the inflaton field happening to have large potential values in this region during the time when most of the expansion inhomogeneity is generated. After a volume expansion of about 100, further expansion is rather homogeneous, and the $\sqrt{h}$ profile stays the same (see Fig. 10).

The extrinsic curvature K is related to the rate of change in $\sqrt{h}$. In Fig. 11 large absolute values of K in the region of large $\sqrt{h}$ are seen. Later K becomes rather homogeneous (see Fig. 12). Regions of largest intrinsic curvature R (Fig. 13) seem to be at or around regions of small expansion. This is partly because in this run those are more pronounced than regions of large expansion, partly because expansion decreases R by increasing the

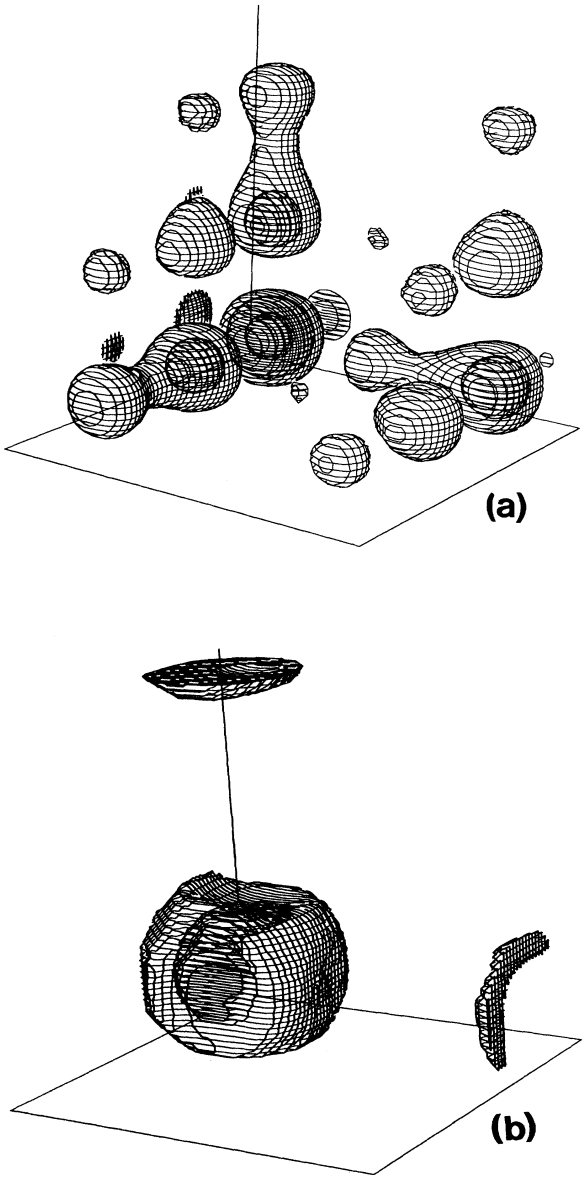

FIG. 9. The local volume expansion $\sqrt{h}$ at $t = 9.2t_{\rm Pl}$. (a) Regions of small $\sqrt{h}$ are enclosed by 30%, 70%, and 83% contours. (b) Regions of large $\sqrt{h}$ are enclosed by 94% and 98% contours.

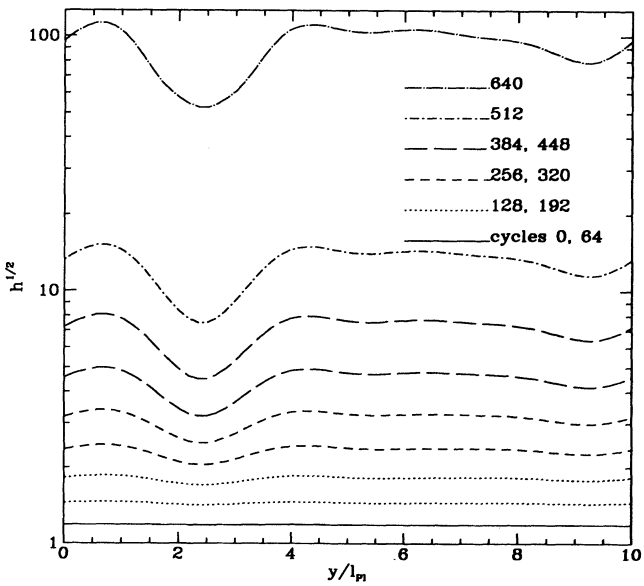

FIG. 10. Same as Fig. 7 but for $\sqrt{h}$.

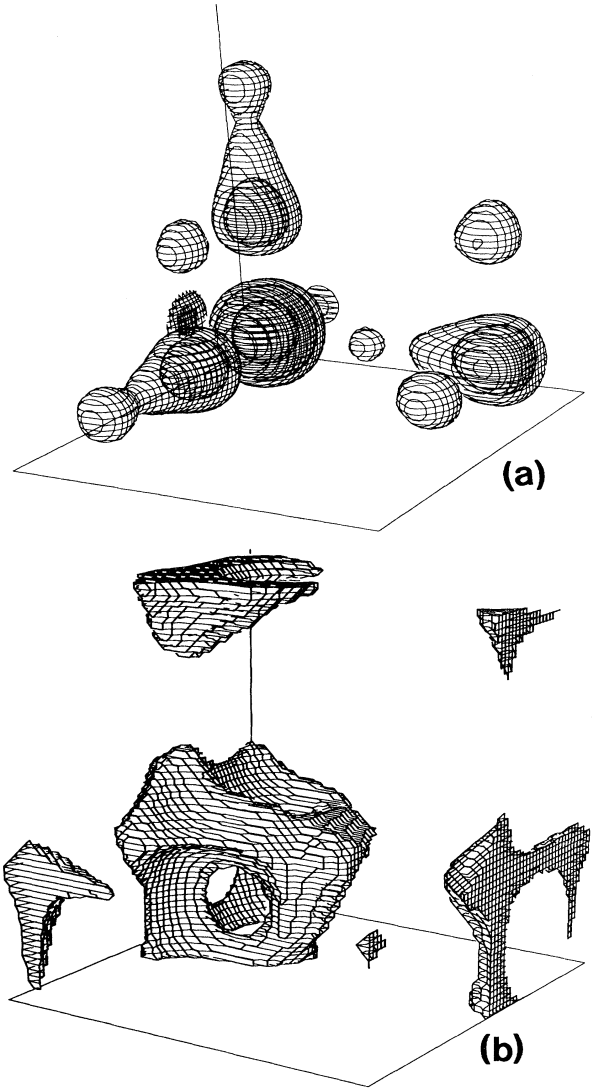

FIG. 11. Trace of the extrinsic curvature at $t=9.2t_{\rm Pl}$. (a) Small values of $|K|$ are enclosed by 50%, 80%, and 88% contours. (b) Large values of $|K|$ are enclosed by the 98% contour.

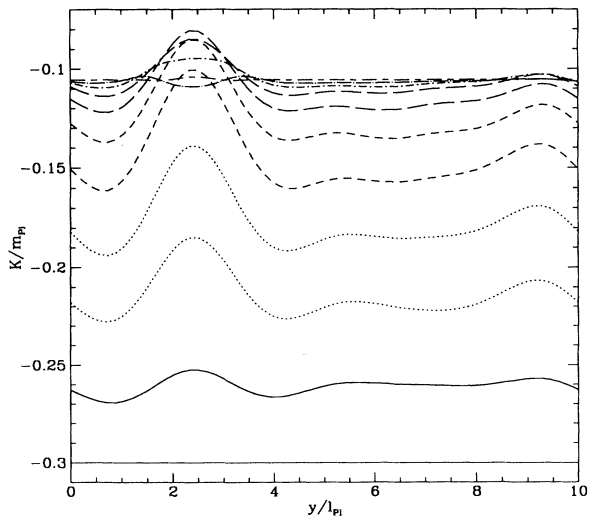

FIG. 12. Same as Fig. 7 but for K.

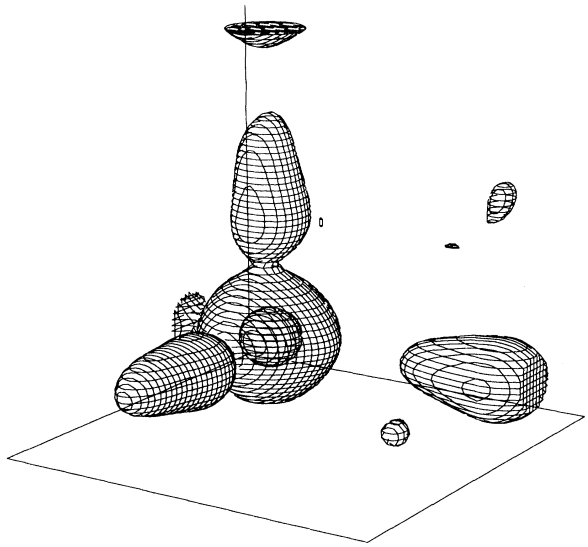

FIG. 13. Scalar curvature at $t=9.2t_{\rm Pl}$. Regions of large R are enclosed by 25% and 75% contours.

curvature radius. Figure 14 shows R along our reference line at different times.

We show only the early part of this run, since the later evolution is less interesting. The inflaton rolls down its potential staying rather homogeneous. Inflation ends as ϕ reaches the bottom and begins to oscillate.

In the large-scale run the inhomogeneities are outside the horizon. They do not oscillate. Rather, they maintain their shape without damping. After a few Hubble times the regions of low (Fig. 15) and high ϕ look very much the same as initially (Fig. 6). Figure 16 shows ϕ along the reference line at various times through the entire run past the end of inflation. We see that aside from the flattening of the sharp initial minimum, the inhomo-

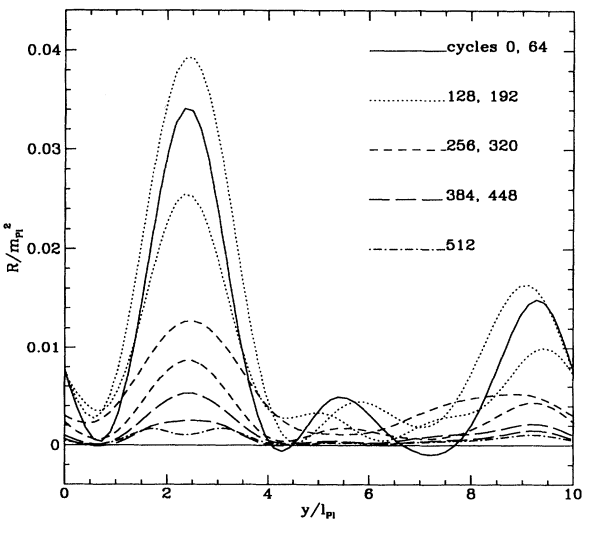

FIG. 14. Same as Fig. 7 but for R.

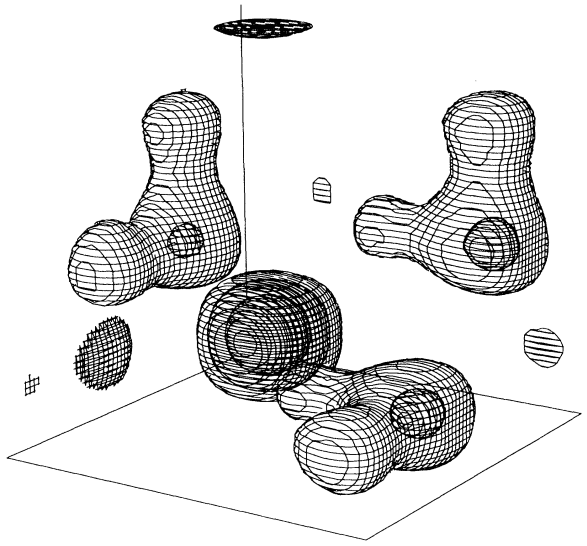

FIG. 15. Figures 15–20 show results from the large-scale run. This figure shows the inflaton field at cycle 512, or $t=166t_{\rm Pl}$, after about 6 Hubble times. Regions of small ϕ are enclosed by 15%, 34%, and 44% contours.

geneity maintains its shape. Because of the larger scale, the Courant condition allows a larger initial time step for this run.

The spatial pattern of the other scalar quantities follows that of ϕ. Larger values of ϕ lead to faster expansion. At first the effect of the other scalar field ϕ_R (see end of Sec. II) shows, but later the regions of the most expansion match those of large ϕ rather closely (Fig. 17). Since the regions of large ϕ and high inflation stay the same, the inhomogeneity in the expansion becomes steeper and steeper (Fig. 18). When inflation ends, some regions have expanded by a volume factor of more than 10^{130}, while others have expanded by less than 10^{75}.

For the extrinsic curvature we show just the 1D plot (Fig. 19). The 3D plots would look intermediate between the ϕ and $\sqrt{h}$ plots. Note the correspondence between Figs. 16, 18, and 19. Larger ϕ, and thus $V(\phi)$, means fas-

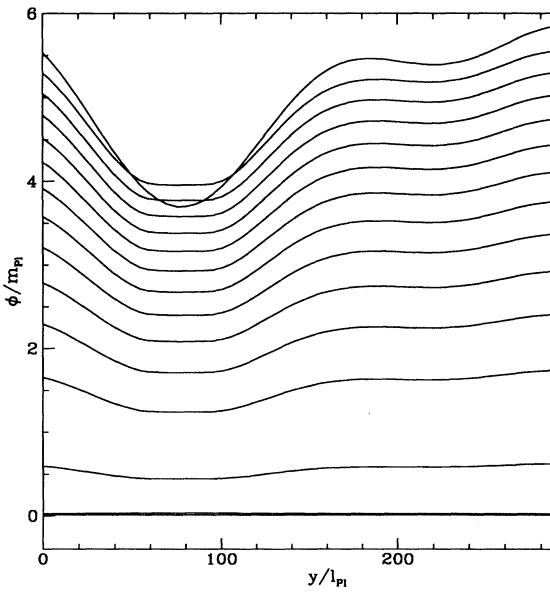

FIG. 16. The inflaton field along the reference line at every 512th cycle. The initial slice is at the top, and the last slices at the bottom, as ϕ moves down with time. The slices shown correspond to $t/t_{\rm Pl}=5$, 166, 482, 598, 852, 1140, 1471, 1861, 2337, 2947, 3797, 5201, 9624, 6.02×10^4, and 7.10×10^5. Defining the end of inflation as the time when $V(\phi)$ falls below 50% of the total energy, it happens at $t=1.2\times10^4t_{\rm Pl}$. The run contains four periods of postinflation oscillations. The last two slices shown (close to each other) are from this era.

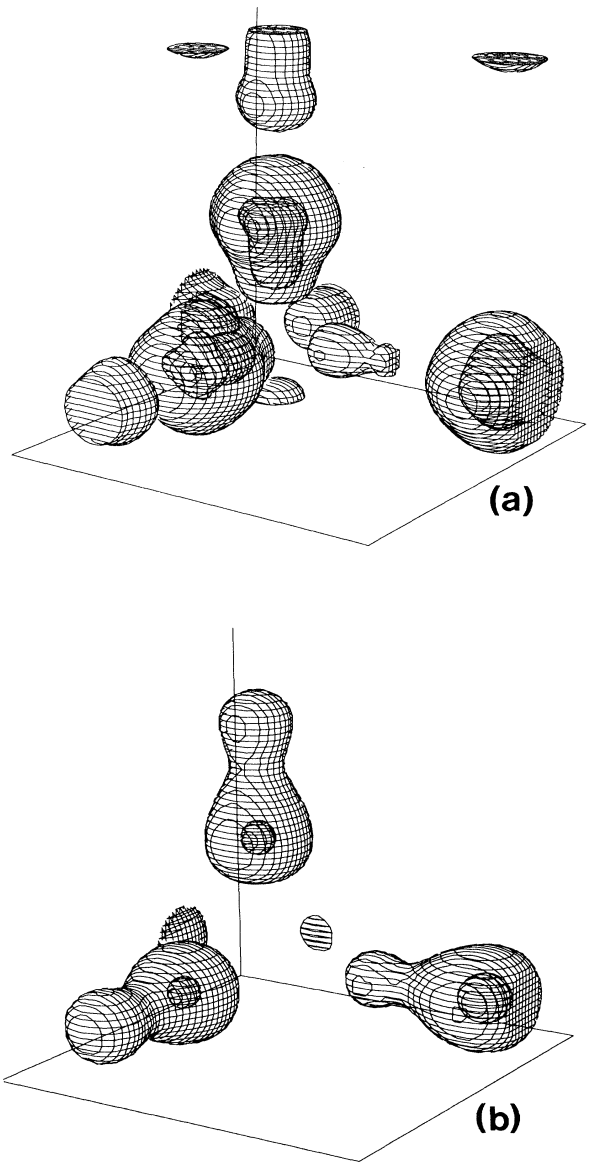

FIG. 17. The local volume expansion $\sqrt{h}$. (a) At cycle 64 or $t=14.7t_{\rm Pl}$. Regions of large $\sqrt{h}$ are enclosed by 60% and 80% contours. (b) At cycle 512 or $t=166t_{\rm Pl}$. Regions of large $\sqrt{h}$ are enclosed by 5% and 50% contours.

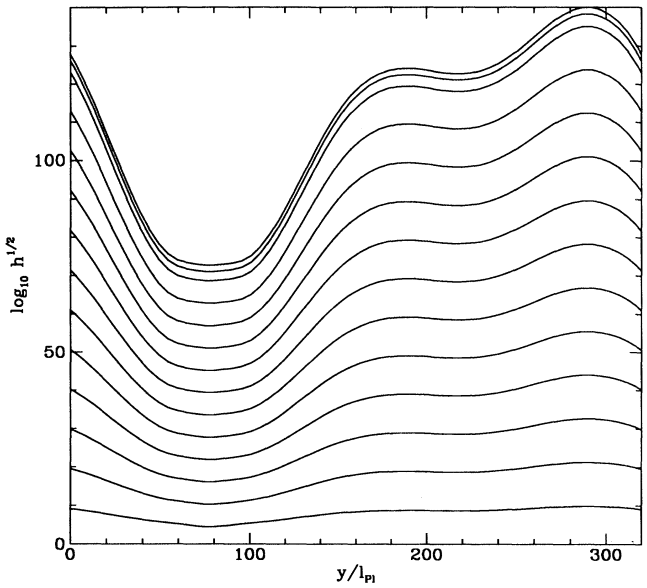

FIG. 18. Same as Fig. 16 but for $\sqrt{h}$. $\sqrt{h}$ moves up with time.

ter expansion, i.e., larger (more negative) K. This then builds up as a larger cumulative expansion $\sqrt{h}$.

In Fig. 20 we show regions of large positive and negative three-curvature R at cycle 64, after half a Hubble time of evolution. The largest curvature is at the region where the expansion has been the smallest. This region of large positive curvature is surrounded by a shell of negative curvature. After more inflation, the curvature decreases but the relative contrast between large- and small-curvature regions increases, so that later contour plots would pick up only the largest-curvature region near the back corner.

The Hamiltonian and momentum constraints were monitored during the evolution. During the small-scale run the maximum errors (root-mean-square relative difference between the left and right sides) were Hamiltonian 0.2% and momentum 3.3%. In the large-scale run these errors were smaller: Hamiltonian 0.05%, momentum 0.3%. We ran these runs also with a coarser grid. Going from a 32^3 grid to the 64^3 grid, the Hamiltonian error went down to about one-quarter, the momentum error to about one-half.

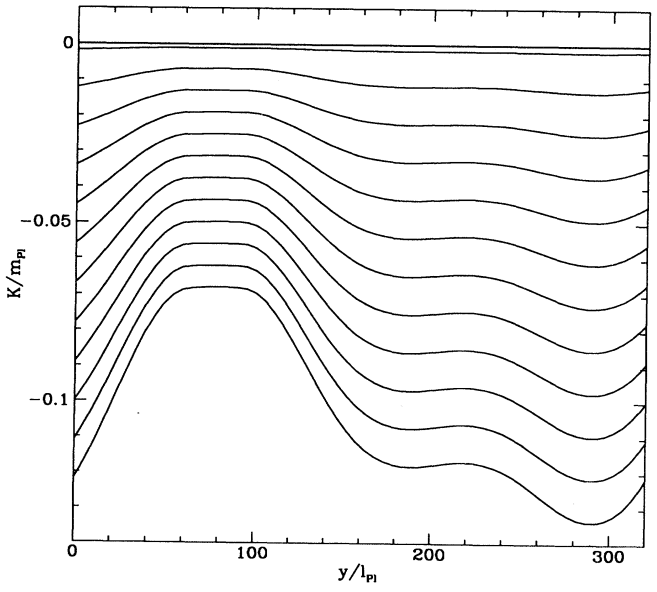

FIG. 19. Same as Fig. 16 but for K. K moves up with time. The initial slice, where K is homogeneous, falls below the area plotted.

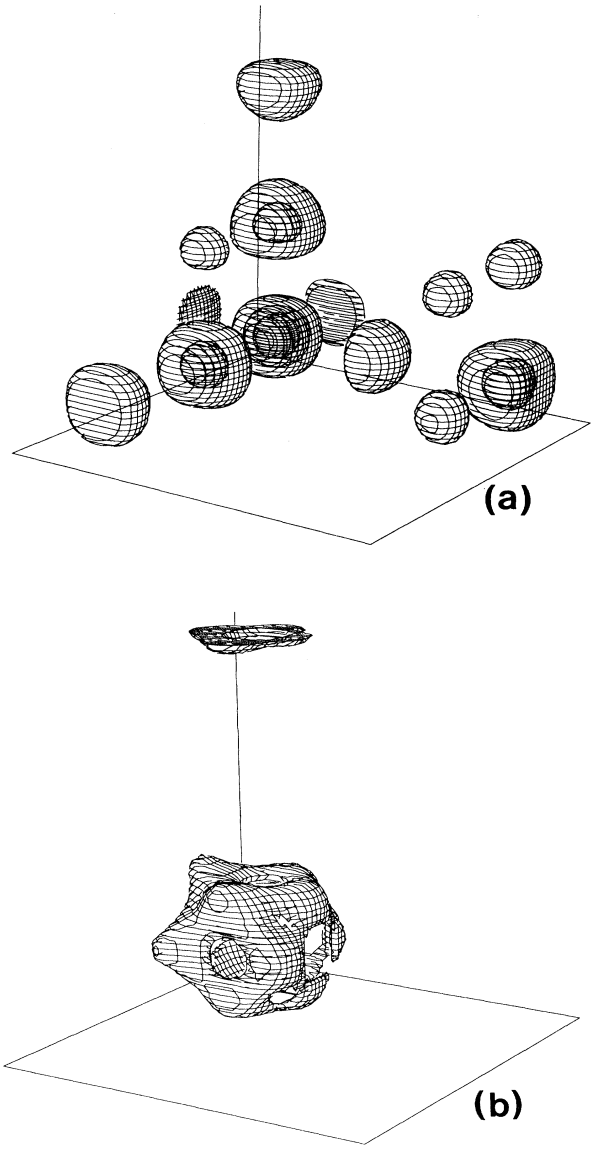

FIG. 20. Scalar curvature at $t = 14.7 t_{Pl}$. (a) Regions of large positive R enclosed by 15%, 30%, and 50% contours ($R = 0.15 \times 10^{-3} m_{Pl}^2$, $0.55 \times 10^{-3} m_{Pl}^2$, $1.10 \times 10^{-3} m_{Pl}^2$). (b) Regions of negative R enclosed by the 3.7% contour ($R = -0.16 \times 10^{-3}$).

VI. CONCLUSIONS

We have created a working, truly three-dimensional, numerical relativity code for studying inhomogeneous inflation. The code has been tested against perturbation theory with good results. On Cray Y-MP computers, a practical grid size to run the code with is around 48^3–64^3. This is enough to handle an interesting amount of structure with reasonable accuracy (but just barely). Present memory limits would allow larger grids, but the increased computation time leads to much worse throughput.

A variant of this code is being used [13] at present for interacting black-hole studies, with initial data computed as described by Cook *et al.* [14], and with asymptotically flat (rather than periodic or reflective) boundary conditions. Sizes at least up to 128^3 are being implemented on a CM-5 computer [15]. We are working also to move the cosmology code to this machine where it will be run with inflaton and with other sources, to describe a number of three-dimensional physical situations.

One of the main motivations for the inflationary scenario was to explain the large-scale homogeneity and isotropy of the Universe without requiring these properties as initial conditions [16]. An apparent shortcoming in the main body of work on inflation is then, that it has nevertheless been in the context of homogeneous space or small perturbations around it. We have now presented numerical simulations of inhomogeneous inflation, where the inhomogeneity has been truly three-dimensional and nonperturbative. These runs had sufficient inflation to solve the standard cosmological conundra. In particular, they contain regions where evidence of the initial inhomogeneity would not be locally observable. We have thus demonstrated the viability of inflation with inhomogeneous initial conditions.

ACKNOWLEDGMENTS

Computations were carried out at the National Center for Supercomputing Applications, University of Illinois at Urbana-Champaign. This work was performed in part under the auspices of the U.S. Department of Energy by the Lawrence Livermore National Laboratory under Contract No. W-7405-ENG-48, and supported in part by NSF PHY8806567. The work by R.A.M. was supported also by a Cray Research University grant, and by Texas Advanced Research Program Grant No. ARP-085.

[1] A. Guth, Phys. Rev. D **23**, 347 (1981).
[2] K. A. Olive, Phys. Rep. **190**, 307 (1990).
[3] G. F. Smoot *et al.*, Astrophys. J. **396**, L1 (1992).
[4] H. Kurki-Suonio, J. Centrella, R. A. Matzner, and J. R. Wilson, Phys. Rev. D **35**, 435 (1987).
[5] K. A. Holcomb, S. J. Park, and E. T. Vishniac, Phys. Rev. D **39**, 1058 (1989).
[6] D. Goldwirth and T. Piran, Phys. Rev. D **40**, 3263 (1989).
[7] D. Goldwirth and T. Piran, Phys. Rev. Lett. **64**, 2852 (1990).
[8] P. Laguna, H. Kurki-Suonio, and R. A. Matzner, Phys. Rev. D **44**, 3077 (1991).
[9] C. W. Misner, K. S. Thorne, and J. A. Wheeler, *Gravitation* (Freeman, San Francisco, 1973).
[10] A. D. Linde, Phys. Lett. **129B**, 177 (1983).
[11] R. Brandenberger, R. Kahn, and W. H. Press, Phys. Rev. D **28**, 1809 (1983); R. Brandenberger and R. Kahn, *ibid.* **29**, 2172 (1984); R. H. Brandenberger, Rev. Mod. Phys. **57**, 1 (1985).
[12] P. Laguna, H. Kurki-Suonio, and R. A. Matzner, in *Sixth Marcel Grossmann Meeting on General Relativity,* Kyoto, Japan, 1991, edited by H. Sato and T. Nakamura (World Scientific, Singapore, 1992), p. 1343.
[13] P. Laguna, H. Kurki-Suonio, and R. A Matzner (unpublished).
[14] G. R. Cook, M. W. Choptuik, M. R. Dubal, S. Klasky, R. A. Matzner, and S. R. Oliveira, Phys. Rev. D **47**, 1471 (1993).
[15] L. Smarr (private communication).
[16] D. S. Goldwirth and T. Piran, Phys. Rep. **214**, 223 (1992).